JOURNAL OF GEOPHYSICAL RESEARCH, VOL. 104, NO. B7, PAGES 15,005–15,023, JULY 10, 1999

Dynamics of a phase change at the base of the mantle consistent with seismological observations

Igor Sidorin, Michael Gurnis, and Don V. Helmberger

Seismological Laboratory, California Institute of Technology, Pasadena

Abstract. The phase change model for the origin of the D" seismic discontinuity is tested by comparing the results of convection modeling with seismic observations. We compute a number of global dynamic models that incorporate a phase change at the base of the mantle with different characteristics and transform the resulting temperature field and the distribution of phases to seismic velocities. Over 900 two-dimensional synthetic waveforms are computed for each of the models from which *S*, *ScS*, and *Scd* phases are picked. The distribution of the relative amplitudes and differential travel time residuals for these phases are statistically compared with the distribution of data from four well studied regions (northern Siberia, Alaska, India, and Central America) in a search for the characteristics of a phase transition that best match these seismic observations. We find that the best fit among the models considered is obtained for phase transitions characterized by a Clapeyron slope of ~ 6 MPa K^{-1} and an elevation above the core-mantle boundary of $\sim$ 150 km under adiabatic temperature or 127 GPa and 2650 K on a (P,T) diagram. Dynamic models demonstrate that the value of Clapeyron slope and the density difference between the phases can have significant influence on the dynamics of plumes but probably only a minor influence on the dynamics of subducted slabs. We find that the thermal structure of subducted slabs can be important in giving rise to the seismic triplication; the strongest *Scd* arrivals in our models are observed in the area of subduction. The folding of the slab at the base of the mantle leads to patterns in differential travel time distributions consistent with seismic observations and suggests that the largest heterogeneity occurs at the top of the D" layer or just above it. Analysis of the spatial autocorrelation functions of the differential travel time residuals suggests that their characteristic peaks reflect the patterns of slab folding and may provide constraints on the rheology of slabs at the base of the mantle.

1. Introduction

The seismologically observed heterogeneity at the bottom 200-300 km of the mantle constituting the D" region is becoming increasingly apparent. The amplitudes of seismic velocity anomalies can exceed 10% for both P and S waves, and the scales of the anomalies range from several tens to several thousand kilometers. This structural complexity probably reflects a variety of interacting geophysical processes that take place in the core-mantle boundary (CMB) region and are believed to play a major role in global dynamics [see *Lay et al.*, 1998]. Interpreting the seismic structure at the base of the mantle provides a key to understanding the dynamic complexity and ultimately the evolution of the Earth as a whole.

Paper number 1999JB900065.
0148-0227/99/1999JB900065$09.00

The large-scale structure of the mantle has been established using long-period tomography techniques [e.g., *Dziewonski and Woodhouse*, 1987; *Su et al.*, 1994; *Li and Romanowicz*, 1996; *Masters et al.*, 1996]. Although some differences exist between various models, several large-scale features in the deep mantle are common to most studies. These include broad low-velocity zones beneath Africa and the Pacific and a relatively fast circum-Pacific fringe. The sharpness of these large-scale features and the lateral transitions between the regions with fast and slow velocities remain unresolved.

Higher resolution can be obtained by using body wave tomography. In some regions, such as beneath the Americas, the ray path coverage is sufficient to image structures in the deep mantle with dimensions within a few hundred kilometers. A tomography model computed by *Grand* [1994] using S body wave data displays narrow, linear, high-velocity features for several regions beneath the circum-Pacific belt. This picture is corroborated by a detailed P wave tomography study [*van der*

Hilst et al., 1997] that employed completely different data types and methods. In addition, the same features are found in the mid mantle using high-resolution surface wave overtones [*van Heijst and Woodhouse*, 1999]. In some regions these fast velocity structures can be traced from the surface to the base of the mantle [*van der Hilst et al.*, 1997], and their morphology has some similarities with the thermal structure of subducting slabs obtained in convection modeling [e.g., *Bunge et al.*, 1998], suggesting that these structures represent the lithosphere subducting to the bottom of the mantle.

Mapping of even smaller variations at the base of the mantle has been achieved by modeling the differential waveform behavior of phases interacting with D" and the CMB. Such studies have revealed ultralow velocity zones with large reductions in both P and S velocities beneath the mid-Pacific, Africa, and other regions [see *Lay et al.*, 1998]. These structures appear to be related to the larger-scale low-velocity zones, as discussed by *Garnero and Helmberger* [1995].

In contrast, the large-scale high-velocity zones appear to have a positive velocity jump at the top of the D" region, as was first suggested by *Lay and Helmberger* [1983]. The primary evidence for this D" discontinuity is based on an extra phase (*Scd*) that arrives between S and ScS at epicentral distances from 65° to 85°, forming a triplication. The triplication is also observed for P waves in some regions; however, the low signal to noise ratio in P waveforms significantly complicates its detection [e.g., *Ding and Helmberger*, 1997]. The timing and amplitude of *Scd* relative to S and ScS show considerable variations [see *Wysession et al.*, 1998]. Four regions that have been well studied and where *Scd* is clearly displayed are indicated in Plate 1 along with the inferred one-dimensional (1-D) velocity models. Model SGLE [*Gaherty and Lay*, 1992] is a reference model for the ray paths under northern Siberia, SYLO [*Young and Lay*, 1990] is for the ray paths under Alaska, SYL1 [*Young and Lay*, 1987] is for the ray paths under India, and SLHA [*Lay and Helmberger*, 1983] for the ray paths under Central America. Because of existing trade offs, such 1-D reference models are not unique [*Sidorin et al.*,

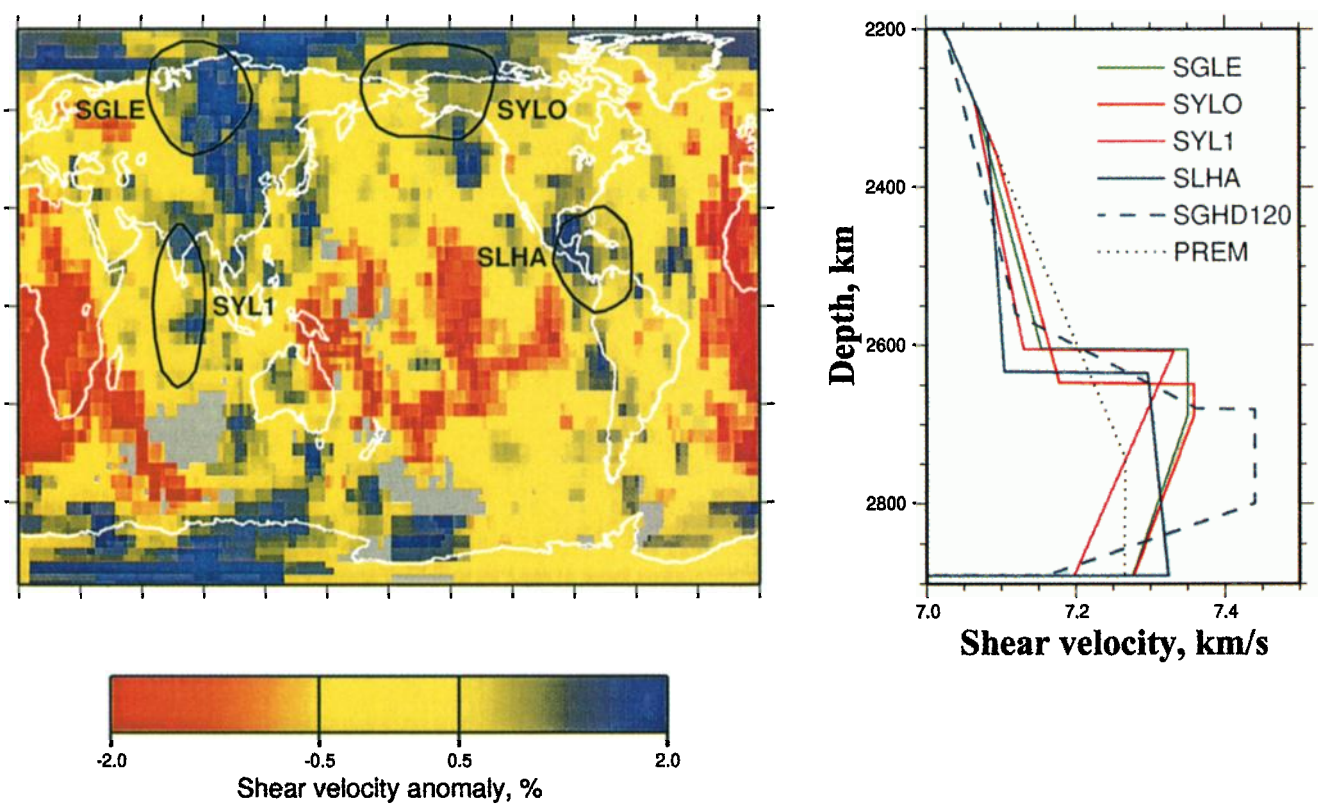

Plate 1. Location of the four geographical regions where there is a strong evidence for the D" triplication. The map shows the average shear velocity anomaly in the lowermost 300 km of the mantle [*Grand et al.*, 1997]. The reference one-dimensional (1-D) models corresponding to the four regions along with the preliminary reference Earth model (PREM) are given on the right: SGLE [*Gaherty and Lay*, 1982] is a reference model for the structure beneath northern Siberia; SYLO [*Young and Lay*, 1990] is for the structure beneath Alaska; SYL1 [*Young and Lay*, 1987] is for the structure beneath India and the Indian Ocean; SLHA [*Lay and Helmberger*, 1983] is for the structure beneath Central America. Model SGHD120 [*Sidorin et al.*, 1998] approximates the structure beneath Central America using a 1% discontinuity and a 120 km transition zone above it. PREM [*Dziewonski and Anderson*, 1981] is a global Earth reference model.

1998]. For example, several different 1-D models have been proposed to approximate the structure beneath Central America [*Lay and Helmberger,* 1983; *Kendall and Nangini,* 1996; *Ding and Helmberger,* 1997; *Sidorin et al.,* 1998]. Two of them, SLHA and SGHD120, are shown in Plate 1. While model SLHA has a 2.75% jump at the top of D", common to most models explaining the triplication, in the structure approximated by model SGHD120 a similar triplication arises because of only a 1% discontinuity overlain by a 120 km transition zone with a high gradient [*Sidorin et al.,* 1998]. However, even considering the uncertainty in such models, they illustrate some of the variability observed around the circum-Pacific belt.

A recent study by *Lay et al.* [1997] addressed these variations in the structure of the D" discontinuity considering the correlations and spatial patterns in *Scd-S*, *ScS-Scd*, and *ScS-S* differential travel time residuals for ray paths sampling the lowermost mantle in three different regions of the world. The study suggested a strong lateral heterogeneity at scale lengths of 600-1500 km at the base of the mantle with significant heterogeneity at smaller (200-500 km laterally) scales. The strongest heterogeneity was prescribed to the region just above or within the top thin layer of D". Although these observations alone may have important dynamic implications, the analysis was unable to distinguish between the volumetric velocity anomalies and the topography of the D" discontinuity. Even when the velocity structure is well constrained, it does not allow a unique determination of the variation of material properties, such as elastic moduli, density, or viscosity, all of which to some extent control the dynamics of mantle flow. The data that are used to study the D" seismic structure, for example, are either not sensitive to the density variations (as *SH* reflections off the discontinuity) or are heavily contaminated by either noise or superposition of other phases (as *SV* or *P* reflections). Consequently, seismological modeling fails to distinguish between thermal and compositional influences on the velocity field.

To provide further constraints on the system, a multidisciplinary approach is required, where dynamically consistent seismic velocity predictions are compared with the seismological observations. Dynamic models that are able to reproduce the seismologically observed general trends and behavior of the seismic travel times and amplitudes, while still not unique, can significantly narrow the range of possibilities for the dynamic mechanisms responsible for certain seismic features, such as the D" discontinuity. Moreover, the dynamic models can also suggest which new or additional seismological observations can be made to distinguish between competing models.

Following such an approach, *Sidorin and Gurnis* [1998] presented a technique to predict seismic velocities consistent with dynamics, experimental mineral physics, and geochemical constraints. *Sidorin et al.* [1998] then used this technique to produce radial seismic velocity profiles for three classes of dynamic models simulating different mechanisms for the origin of the D" discontinuity. The velocity profiles were used to produce SH synthetics, which were analyzed for the presence of the *Scd* phase. They demonstrated that thermal gradients from subducted slabs alone atop the CMB cannot produce a sufficiently strong *Scd* arrival. A chemical layer model with a sufficient velocity contrast can cause a strong triplication, but the geographical pattern of the strength of the arrivals and the depth of the discontinuity are opposite to the seismological observations: in the seismically fast regions associated with a subducted slab the model predicts a very weak *Scd* phase, and the discontinuity is depressed relative to the slow regions, where *Scd* arrivals are strong. The study favored a solid-solid phase change model and demonstrated that such a model with a velocity contrast of just 1% can predict both the geographical pattern and the amplitudes of the arrivals consistent with observations.

In this study we elaborate on the work of *Sidorin et al.* [1998] by modeling the dynamics of a phase change at the top of D". We consider a range of convection models with different characteristics of the phase change. The results of the convection calculations are used to produce seismic velocity fields. We then generate 2-D synthetics and analyze the waveforms for the presence of *Scd* phase, its lateral variations, and its correlation with dynamic features. Because of the complexity of both the modeled and observed wave trains, we choose a statistical approach to compare the predicted relative amplitudes and differential travel times with the seismological observations. The predicted scale lengths of the heterogeneity in the computed velocity models are compared with those observed by *Lay et al.* [1997] in different regions of the world. This analysis is used to reject certain models and to select a class of models with the characteristics of the phase change that dynamically produce the most seismologically consistent velocity fields.

2. Dynamic Models

We compute a variety of cases of convection models in a 2-D cylindrical coordinate system (r, ϕ). A solid-solid phase change is introduced close to the bottom of the model domain, with its characteristics varying between model cases. In the Boussinesq approximation of an incompressible fluid the governing nondimensional equations are

$$\nabla \cdot (\mu \nabla \boldsymbol{u}) = -\nabla p + \frac{1}{\zeta^3}\alpha(r) Ra \left(T - \frac{1}{\alpha(r)} B_{\mathrm{ph}}\, \Gamma_{\mathrm{ph}} \right) \hat{\boldsymbol{r}} \quad (1)$$

$$\frac{\partial T}{\partial t} = -(\boldsymbol{u} \cdot \nabla) T + \nabla^2 T + H \quad (2)$$

$$\nabla \cdot \boldsymbol{u} = 0 \quad (3)$$

where all the quantities are dimensionless and $\boldsymbol{u}$ is velocity, r is radius, $\hat{\boldsymbol{r}}$ is a unit vector in the radial direction, p is pressure, T is temperature, t is time, μ is dynamic viscosity, α is the coefficient of thermal expansion, and ζ is the depth of the core-mantle boundary. We do not consider the effects of internal heating in this study and assume $H = 0$ in (2).

In (1), $\Gamma_{\rm ph}$ is a function that characterizes the phase of the mantle material at a particular location and can take values from 0, corresponding to the ambient, low-pressure phase, to 1, corresponding to the high-pressure phase. It can be written as [*Christensen and Yuen*, 1984]

$$\Gamma_{\rm ph}(r,\phi) = \frac{1}{2}\left[1 + \tanh\left(\frac{1}{w_{\rm ph}} r_{\rm ph}\right)\right] \tag{4}$$

where $w_{\rm ph}$ is the nondimensional width of the phase transition and $r_{\rm ph}$ is given by

$$r_{\rm ph}(r,\phi) = (1-r) - (\zeta - h_{\rm ph}) - \gamma_{\rm ph}\left[T(r,\phi) - T_{\rm ph}\right] \tag{5}$$

In (5), $h_{\rm ph}$ is the dimensionless elevation of the phase change above the CMB corresponding to dimensionless temperature $T_{\rm ph}$, and $\gamma_{\rm ph}$ is the dimensionless Clapeyron ratio.

Dimensionless parameters r, $\boldsymbol{u}$, p, T, t, μ, and α in (1)–(3) and $w_{\rm ph}$, $h_{\rm ph}$, $T_{\rm ph}$, and $\gamma_{\rm ph}$ in (4)–(5) refer to the corresponding dimensional values by means of the following scaling relations:

$$r^* = R_0 r, \tag{6}$$

$$\boldsymbol{u}^* = \frac{\kappa}{R_0}\boldsymbol{u}, \tag{7}$$

$$p^* = \frac{\kappa\bar{\mu}}{R_0^2} p \tag{8}$$

$$T^* = T_S + \Delta T\, T \tag{9}$$

$$t^* = \frac{R_0^2}{\kappa} t \tag{10}$$

$$\mu^* = \bar{\mu}\mu \tag{11}$$

$$\alpha^* = \bar{\alpha}\alpha \tag{12}$$

$$w_{\rm ph}^* = R_0 w_{\rm ph} \tag{13}$$

$$h_{\rm ph}^* = R_0 h_{\rm ph} \tag{14}$$

$$T_{\rm ph}^* = T_S + \Delta T T_{\rm ph} \tag{15}$$

$$\gamma_{\rm ph}^* = \frac{\rho_0 g R_0}{\Delta T}\gamma_{\rm ph} \tag{16}$$

where R_0 is the radius of the Earth, κ is the thermal diffusivity, $\bar{\mu}$ and $\bar{\alpha}$ are the volume-averaged mantle viscosity and thermal expansivity, respectively, ΔT is the nonadiabatic temperature increase across the mantle, T_S is the temperature at the surface of the Earth, ρ_0 is the average mantle density, and g is the gravitational acceleration (Table 1). Asterisks in (6)–(16) denote dimensional values and will be dropped in all subsequent equations for clarity.

Parameter Ra in (1) is the thermal Rayleigh number that characterizes the vigor of convection of the system and is given by

$$Ra = \frac{g\bar{\alpha}\rho_0 \Delta T D^3}{\kappa\bar{\mu}} \tag{17}$$

where D is the depth of the core-mantle boundary (Table 1). Parameter $B_{\rm ph}$ in (1) characterizes the intrinsic buoyancy of the high-pressure phase with respect to the thermal buoyancy and is given by

$$B_{\rm ph} = \frac{\Delta\rho_{\rm ph}}{\rho_0\bar{\alpha}\Delta T} \tag{18}$$

where $\Delta\rho_{\rm ph}$ is the density increase associated with the transition to the high-pressure phase.

Calculations are performed for a half annulus (Figure 1), where the inner radius corresponds to the CMB and the outer radius corresponds to the surface of the Earth. Free slip conditions are used at the bottom; reflection boundary conditions are used on the two side walls. At the top, plates are simulated by imposing velocity boundary conditions, where the amplitudes of the plate velocities are determined from a free slip calculation [e.g. *Gurnis and Davies*, 1986]. *Han and Gurnis* [1999] have shown that although such boundary conditions do substantial work on the system, the work is dissipated within the lithosphere. Consequently, the approach is quite adequate for studies including the dynamics of the bulk of the fluid layer. A velocity overshoot is applied in the back arc basin to facilitate subduction and detachment of the slab from the overriding plate [*Christensen*, 1996; *Davies*, 1997]. The sub-

Table 1. Values of Parameters Used in Convection Computations

Parameter	Symbol	Value
Radius of the Earth	R_0	6371 km
Depth of the core-mantle boundary	D	2891 km
Gravity acceleration	g	10 m s^{-2}
Average mantle density	ρ_0	4.0 g cm^{-3}
Average mantle viscosity	$\bar{\mu}$	3.16×10^{21} Pa s
Thermal diffusivity	κ	10^{-6} m^2 s^{-1}
Average thermal expansivity	$\bar{\alpha}$	1.535×10^{-5} K^{-1}
Temperature increase across the mantle	ΔT	2900 K
Velocity of subducting plate	$U_{\rm plate}$	5 cm yr^{-1}
Trench migration velocity	$U_{\rm trench}$	0.5 cm yr^{-1}

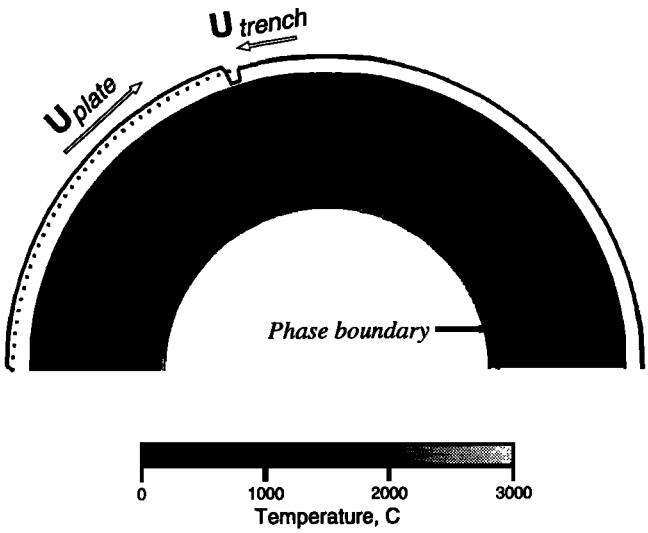

Figure 1. Temperature field after 20 million years of subduction. The imposed surface velocity conditions are indicated at the top (the dotted line shows zero velocity).

ducting plate is moving at $U_{\text{plate}} = 5$ cm yr^{-1} and a trench rollback is added with the migration velocity of the trench $U_{\text{trench}} = 0.5$ cm yr^{-1}. The velocity of the overriding plate is taken equal to U_{trench}.

The mantle is initially isothermal with superimposed top and bottom thermal boundary layers. The thermal boundary layer for the oceanic lithosphere of the subducting plate is computed using an infinite half-space cooling model. The age of the lithosphere at the initial trench location is $\sim$ 160 million years. For the bottom boundary layer and the continental lithosphere (overriding plate) an initial age of 100 million years is used. The total temperature variation across the mantle is $\Delta T = 2900$ K^{-1}, with equal partitioning of the variation between the lower and bottom boundary layers.

The depth dependence of the dimensionless coefficient of thermal expansion is given by

$$\alpha(r) = \frac{2.93}{1 + 10.5(1 - r)^{0.85}} \tag{19}$$

and is consistent with the experimental data for olivine at the surface and predictions of experimental mineral physics for a silicate perovskite and magnesiowüstite assemblage in the lower mantle [*Sidorin and Gurnis*, 1998].

A depth- and temperature-dependent dynamic viscosity μ is used in (1). The depth dependence includes an order of magnitude increase at the 670 km boundary between the upper and lower mantle. The temperature dependent part (Figure 2) is given by

$$\mu(T) = \exp\left(\frac{c_1}{c_2 + T} - \frac{c_1}{c_2 + 0.5}\right) \tag{20}$$

Since stress dependence is expected to reduce significantly the effective viscosity of the subducting lithosphere [*Christensen*, 1984] but is not accounted for in the computations a cutoff of 10 is applied at low temperatures. We use $c_1 = 41.5$ and $c_2 = 0.77$ in (20). These values provide a substantially stronger temperature dependence of viscosity than is used by *Sidorin and Gurnis* [1998], producing a more realistic 4 orders of magnitude variation in the bottom thermal boundary. As in [*Sidorin and Gurnis*, 1998], viscosity is normalized to ensure that the volume average of $\log \mu$ is 0 when averaged over the entire duration of the simulation.

Equations (1)–(3) are solved using a finite element code ConMan [*King et al.*, 1990] which that has been modified for the cylindrical geometry by *Zhong and Gurnis* [1993]. The computations were carried out on a mesh with 400 elements in the azimuthal direction and 100 elements in the radial direction. The mesh was refined both vertically in the top and bottom thermal boundary layers and laterally around the trench, so that the resolution at these regions was $\sim$ 12 km in either direction.

We consider a number of models by varying γ_{ph} from -10 to $+10$ MPa K^{-1} and h_{ph} from 100 to 300 km. In order to produce a sharp seismic discontinuity we use a narrow phase transition with $w_{\text{ph}} = 3$ km. The density change associated with the phase transition is taken to be either 0% (passive phase) or 1%.

All models were integrated for a total time of 340 million years. Plate 2 illustrates the general influence of the basal phase change on the dynamics of the system. In the case of a passive phase change with $\gamma_{\text{ph}} = 6$ MPa K^{-1}, $h_{\text{ph}} = 150$ km (Plate 2a) the phase change does not have any influence on the dynamics but will have a substantial influence on the predicted

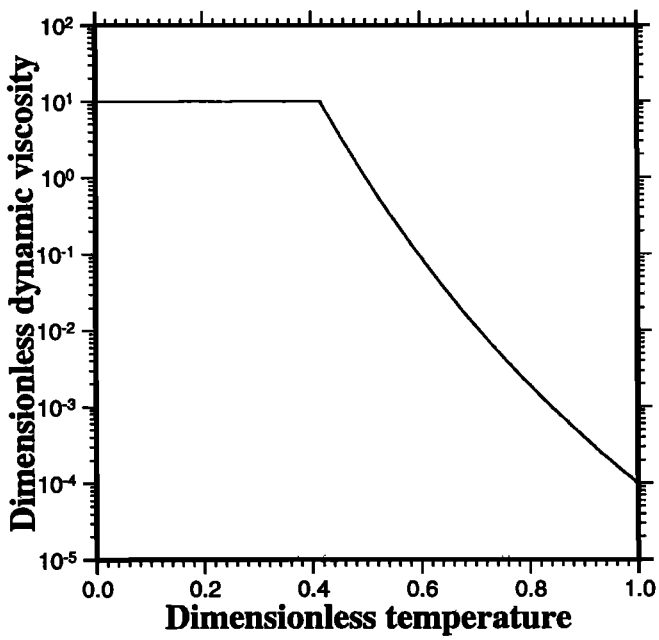

Figure 2. Temperature dependence of viscosity.

seismic signature. As the slab subducts to the base of the mantle, it spreads atop the core-mantle boundary with some folding and buckling developing in the bottom part of the slab. The slab rests almost horizontally at the base of the mantle and is steeply dipping in the mid mantle.

The bottom boundary layer grows in thickness and eventually becomes gravitationally unstable, giving rise to hot plumes. Large plume heads erupting from the CMB and quickly rising to the surface are followed by relatively thin hot tails. In some cases, as a new instability is created in the bottom boundary layer, a new plume head erupts in the same location, following an existing plume tail. In other cases, new plumes erupt from different regions of the CMB with the old tails eventually remixing with the bulk of the flow. The strongest and the most stable (with multiple heads erupting in pulses from approximately the same location at the CMB) plume always seems to emerge just at the tip of the slab. It is also always the first plume to emerge, caused by the local thickening of the hot thermal boundary layer by the slab.

The phase boundary is elevated through the flat-lying slab and reaches its greatest height where the slab first reaches the CMB. In the hot areas the phase boundary is depressed, and the phase transition does not occur in the hot plume tails or when new plume heads erupt from the CMB. The continuity of the boundary becomes intermittent in hot areas with most variation occurring near plumes or the boundary between the flat lying slab and erupting plume.

Our next model has the same value of Clapeyron slope (6 MPa K^{-1}) and elevation of the phase transition above the CMB (150 km), but the high-pressure phase is assumed to be 1% denser than the low-pressure phase. For this model the overall pattern of convection is only moderately changed (Plate 2b). Plumes become stronger and more common, as can be observed in Plate 2b, where after the same time of integration a second plume head has emerged at the tip of the slab and the head of the rightmost plume is much wider and spread beneath the surface than in the case of a passive phase change (Plate 2a). On the other hand the effect of a greater phase density on the subducting slab is subtle. This is probably explained by the high viscosity of the slab and the continuity of the plate tectonic model, which continuously supplies a substantial amount of negative buoyancy at a steady rate. The strength of the basal phase change only weakly influences the driving force on the lower mantle slab.

Using a negative Clapeyron slope $\gamma_{ph} = -6$ MPa K^{-1} with a 1% density contrast (Plate 2c), again, has a limited effect on the dynamics of the slab. However, such a phase change significantly inhibits the formation of plumes. This observation agrees well with the results of a study of *Breuer et al.* [1998] for the Martian mantle, which has been interpreted by them as "thermal barriers" that are created by the phase change due to latent heat consumption. The phase boundary now becomes a global feature, depressed in the cold region associated with the slab but elevated where plumes emerge from the CMB. It generally appears smoother than in the cases of a positive γ_{ph} because of the smoother temperature gradients that exist a few hundred kilometers from the CMB.

3. Synthetic Waveforms

To select a class of dynamic models consistent with seismological observations, we transform the temperature field obtained from the convection models into a seismic velocity field. A PREM-like structure is used for the upper mantle and a technique presented by *Sidorin and Gurnis,* [1998] is applied to compute the elastic parameters and density in the lower mantle (Plate 3). The computations start from an adiabatic model of the lower mantle, obtained to provide the best fit to PREM and based on the mineral physics data and geochemical constraints. The results of convection computations (the temperature field and the distribution of the phases) are then used to add the nonadiabatic perturbations to the adiabatic parameters. Following the results of *Sidorin et al.,* [1998], we assume a 1% shear velocity increase across the phase boundary. As the shear velocity is controlled by both density ρ and shear modulus G different changes in the shear modulus are required for a passive and a denser phase change to provide a 1% velocity jump. We estimated that a roughly 2% jump in shear modulus is needed for cases with no density difference between the phases, and 3% jump is needed for a 1% density change.

Using the computed seismic velocity fields, we produce synthetic waveforms that are compared with the observations. We limit our analysis to the horizontally polarized shear wave (SH) as some of the best seismological observations of the D" triplication pertain to the Scd_H phase. A combination of a modified WKBJ (WKM) method and generalized ray theory (GRT) is used to compute the waveforms in a 2-D seismic velocity field [*Ni et al.,* 1999]. A 600 km deep point source is assumed in all computations.

To study the spatial variations of the computed waveforms, we compute waveforms for a set of ray paths with a fixed epicentral distance Δ but with different locations of the source and receiver. This representation of the wave field is widely used in exploration geophysics and is known as a constant offset section. The construction of such a section is illustrated in Plate 3a, where a source-receiver pair with a fixed separation $\Delta = 80°$ is moved around the domain by shifting it by a constant azimuth increment $\Delta\phi = 40°$. Any location of the source-receiver pair can be characterized by the azimuthal coordinate ϕ_{refl} of the ScS bouncing point, and so, the corresponding waveforms can be plotted as a function of ϕ_{refl} that characterizes the location at the CMB that is sampled by the paths. To allow sampling

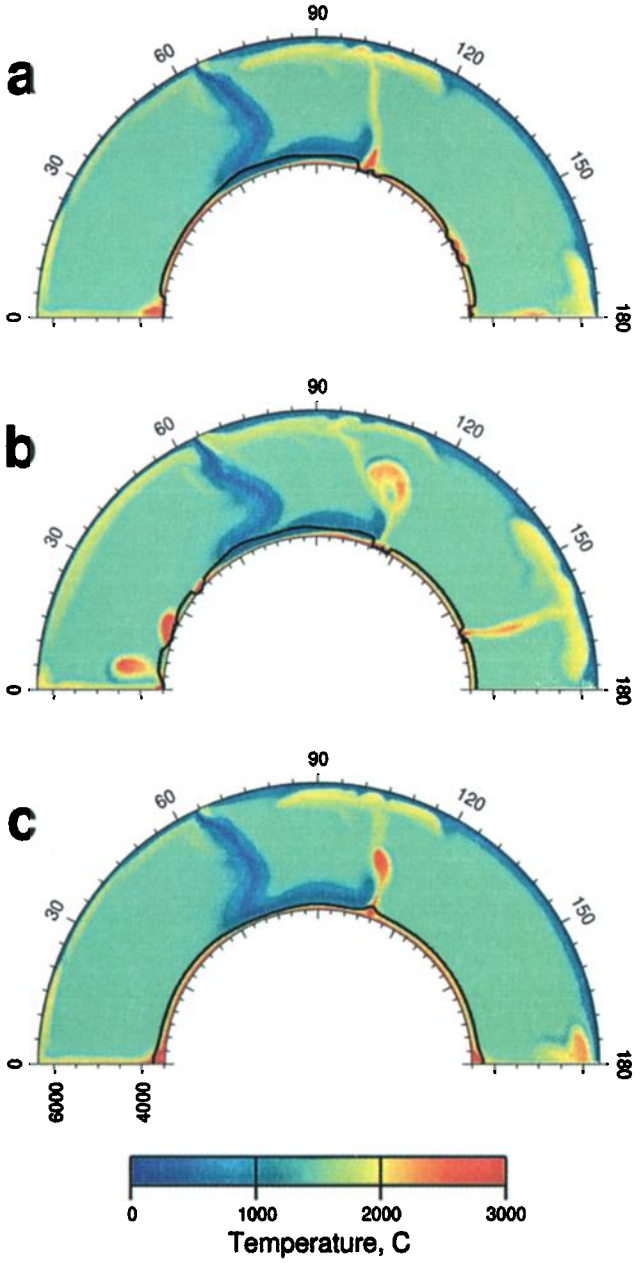

Plate 2. Temperature fields and location of the phase boundary after 340 million years of subduction for three different models: (a) $\Delta\rho_{ph}/\rho_0 = 0$, $\gamma_{ph} = 6$ MPa K^{-1}, and $h_{ph} = 150$ km; (b) $\Delta\rho_{ph}/\rho_0 = 0.01$, $\gamma_{ph} = 6$ MPa K^{-1}, and $h_{ph} = 150$ km; and (c) $\Delta\rho_{ph}/\rho_0 = 0.01$, $\gamma_{ph} = -6$ MPa K^{-1}, and $h_{ph} = 150$ km;

of the deep mantle near the side walls of the model, the seismic velocity field was symmetrically continued to a full annulus in a way consistent with the reflecting boundary conditions used on the side walls in the convection model. This continuation allows us to cover the whole model domain with seismic rays so that ϕ_{refl} can vary from 0° to 180°. We computed constant offset sections for $\Delta = 75°$, 77°, 79°, 81°, and 83° using an azimuth increment $\Delta\phi = 1°$. This set of epicentral distances corresponds to the range where *Scd* is a sufficiently strong arrival and is still distinguishable from the direct arrival.

Three constant offset sections for $\Delta = 75°$, 79° and 83° computed for a model with $\Delta\rho_{ph} = 0$, $\gamma_{ph} = 6$ MPa K^{-1} and $h_{ph} = 150$ km are given in Figure 3, with a part of the section for $\Delta = 79°$ enlarged in Figure 4. The sections clearly show an intermittent D" triplication, with *Scd* arrival being sufficiently strong only in a limited region, primarily in the area with $50° < \phi_{refl} < 100°$. Comparison with the seismic structure in Plate 3a reveals that this area corresponds to a broad fast shear velocity anomaly associated with the subducted slab. Away from the slab, *Scd* can still be observed for $\Delta = 83°$, although with a considerably reduced amplitude, with no trace of an *Scd* found for smaller epicentral distances.

Although lacking the additional complexity of source mechanisms and instrument response, the computed waveforms display strong variations in amplitudes and arrival times of various phases, especially *Scd*. While such variations are commonly observed, it proves difficult to make a direct comparison of the modeling results with the waveform data, and some other technique must be used. We choose a statistical approach here, where the first moments of differential travel times and relative amplitudes distributions are compared for the computed results and data.

To facilitate this comparison, the phases (*S*, *ScS* and *Scd*) are picked automatically (see dashed lines in Figure 4) from the synthetic seismograms using a simple algorithm. The direct phase and phase reflected from the core present no difficulties, while certain problems exist with *Scd* phase. On many waveforms the phase is weak (or completely absent) and may be lost in the noise. In addition, on some waveforms an additional arrival, *St*, is observed (Figure 4) between *S* and *ScS*, linked by *Sidorin et al.* [1998] to the seismic structure produced by thermal gradients within a folding slab. When more than one phase is suggested for *Scd* by the phase-picking algorithm, the one with a significantly higher amplitude or, if the amplitudes are comparable, the sharper phase (the phase with a higher absolute value of acceleration) is accepted. To minimize the erroneous picks, we set a threshold, rejecting an *Scd* pick if the amplitude of the phase is < 10% of the amplitude of the direct arrival.

The first-order moment of the amplitudes and travel time distributions for the data can be characterized by a 1-D seismic velocity reference model that is produced to provide the best fit to the observations. Several such models have been advanced for various regions of the world with clear evidence for a D" triplication. In this study we consider four such regions: northern Siberia, Alaska, India and the Indian Ocean, and Central America, characterized by their respective 1-D reference models SGLE, SYLO, SYL1, and SLHA (Plate 1).

We introduce three parameters, ΔM_1^A, ΔM_1^T and

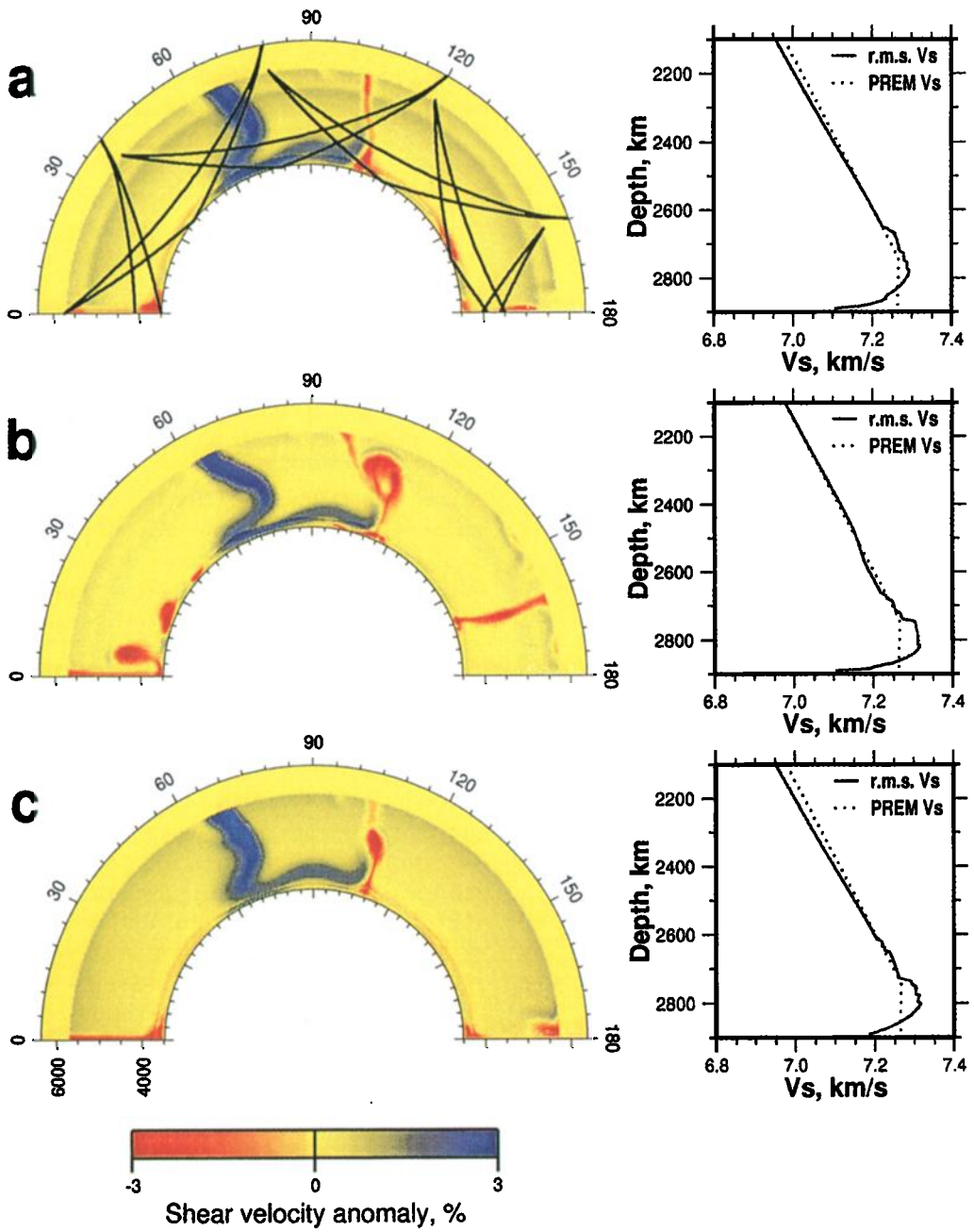

Plate 3. Shear velocities computed for the convection models in Plate 2. A 1% velocity jump is assumed at the phase boundary. A rms value of the shear velocity at each depth (shown on the right with PREM values for a reference) was subtracted to produce the anomaly at any given point plotted on the left. Plate 3a illustrates the procedure used to compute a constant offset section: a source-receiver pair with a fixed separation ($\Delta = 80°$) is shifted by a constant azimuth increment $\Delta\phi$ to compute waveforms for different values of the *ScS* bouncing point ϕ coordinate, ϕ_{refl}; for each location of the source-receiver pair, *S* and *ScS* rays are plotted.

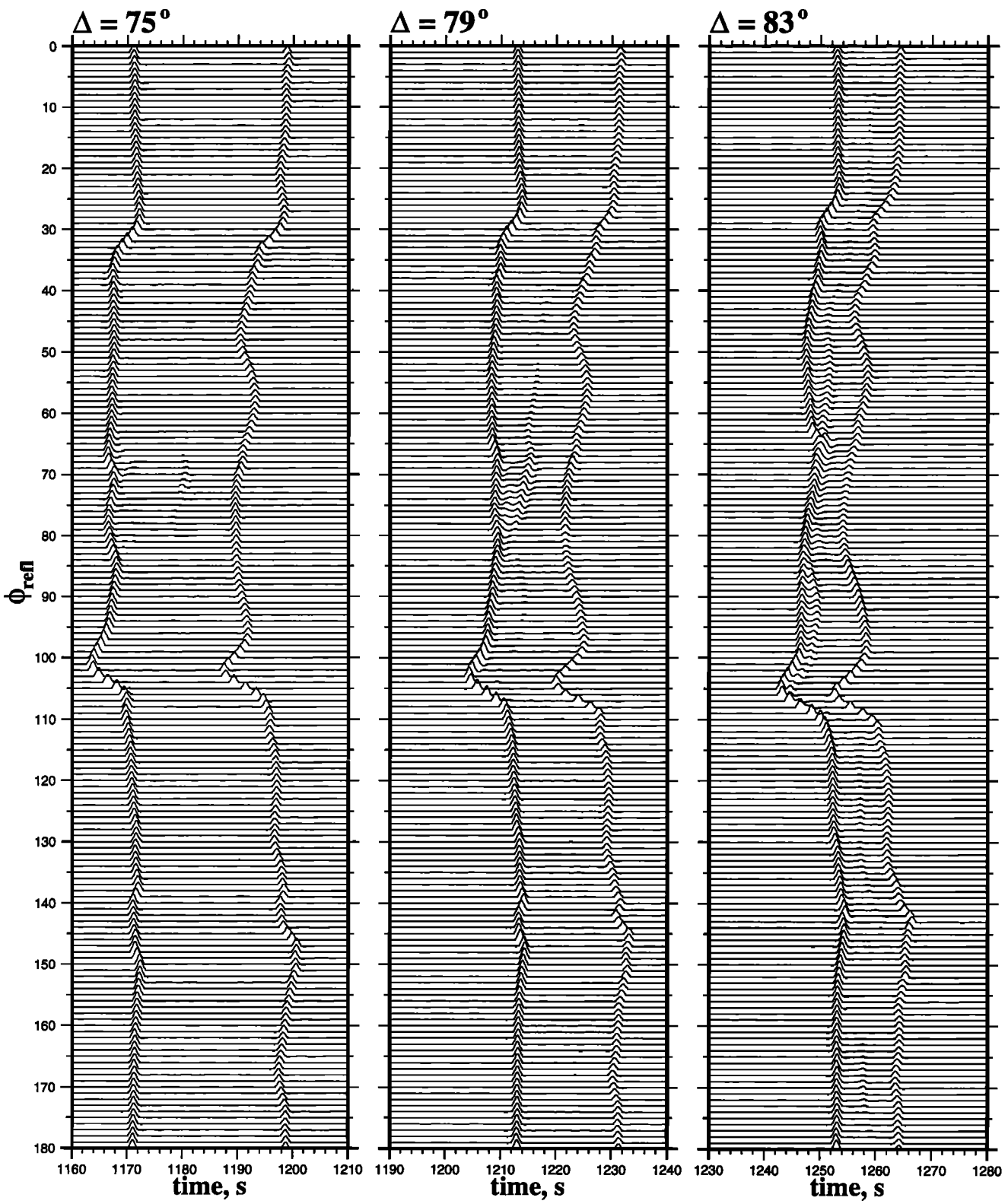

Figure 3. Constant offset sections for (left) $\Delta = 75°$, (middle) $\Delta = 79°$, and (right) $\Delta = 83°$ computed for a model with $\Delta\rho_{ph}/\rho_0 = 0$, $\gamma_{ph} = 6$ MPa K^{-1}, and $h_{ph} = 150$ km. The first arrival is the direct *S*; the last arrival is the core reflection *ScS*. *Scd* arrivals can be observed between *S* and *ScS* in some regions.

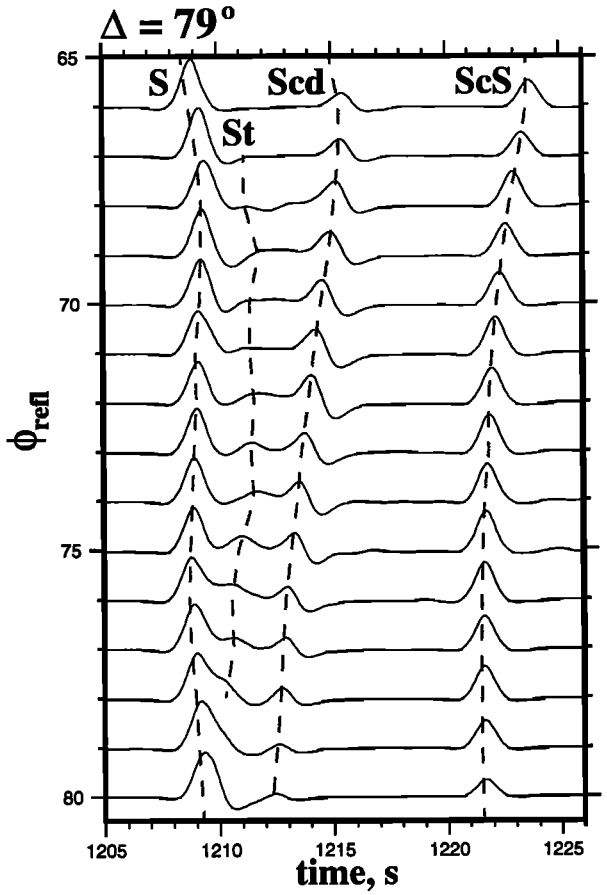

Figure 4. Constant offset section for $\Delta = 79°$ for a model with $\Delta\rho_{ph}/\rho_0 = 0$, $\gamma_{ph} = 6$ MPa K^{-1} and, $h_{ph} = 150$ km, enlarged for $65° \le \phi_{refl} \le 85°$. The four phases (*S*, *St*, *Scd*, and *ScS*) are indicated by the dashed lines (the picks were obtained automatically).

ΔM_2^T, which we use to characterize the overall statistical misfit between the amplitudes and travel times of waveforms produced for a computed model and the data for a given region of the world. Parameter ΔM_1^A will be used to characterize the difference between the first central moments of relative amplitude distributions for the synthetics and the data. Parameters ΔM_1^T and ΔM_2^T will be used to characterize the difference between the first moments and the second moments, respectively, of the differential travel times distributions.

3.1. Comparison of Relative Amplitudes

Figure 5 shows *Scd/S* amplitude ratios computed for the model with a passive phase with $\gamma_{ph} = 6$ MPa K^{-1} and $h_{ph} = 150$ km. The amplitude ratios are normalized by the respective ratios for four different 1-D reference models and are plotted as a function of the *ScS* bounce point coordinate ϕ_{refl}. There are obviously large variations in the relative *Scd* amplitudes, and, at least in some regions these amplitudes are consistent with the relative amplitudes observed for the paths through northern Siberia, Alaska, India, and Central America. Using this observation, we restrict the analysis of the computed models to the range $50° < \phi_{refl} < 90°$. This region in the models corresponds to the most distinct *Scd* arrivals, and its lateral extent is comparable to that of many areas in the world with stable observations of the D" triplication [*Lay et al.*, 1997]. This is also the region of a broad fast velocity anomaly at the base of the mantle caused by the thermal signature of the subducted slab, so that the dynamic context of this region is similar to the four geographical regions that we consider, each of which has either ongoing subduction or has had substantial subduction since the Mesozoic.

No systematic study has yet addressed the *Scd/S* amplitude variations in the waveforms that display the D" triplication. In fact, the effects of the deep structure would be difficult to isolate in such variations because of variable radiation patterns, station effects, and attenuation along the ray paths. Although the relative amplitudes provide weaker constraints on the 1-D reference models than the differential travel times, for the purposes of our analysis we assume that *Scd/S* in the observed waveforms are scattered (with no systematic shift) around the $(Scd/S)_{1D}$ values of the 1-D reference model for the corresponding region, so that $\langle (Scd/S)_{data}/(Scd/S)_{1-D} \rangle = 1$. Using this assumption, we introduce the parameter ΔM_1^A as

$$\Delta M_1^A(\text{model}, \text{refl1D}) = \left| 1 - \left\langle \frac{(Scd/S)_{model}}{(Scd/S)_{refl1D}} \right\rangle \right| \quad (21)$$

Parameter (21) gives a quantitative measure of closeness of the average amplitude ratios for a computed model to those for the real data in a given region (characterized by the 1-D reference model refl1D). Large values of ΔM_1^A correspond to large deviations of relative amplitudes from the 1-D reference model amplitudes that represent the average values for the data in the particular region.

3.2. Comparison of Differential Travel Times

A comprehensive study of the *Scd-S*, *ScS-Scd*, and *ScS-S* differential travel time distribution in three different regions (northern Siberia, Alaska and India) was recently carried out by *Lay et al.* [1997]. It was demonstrated that the differential travel times $(\delta T_X)_{refl1D} = T_X - (T_X)_{refl1D}$ (where X is *Scd-S*, *ScS-Scd*, or *ScS-S*) have a zero mean (first-order moment of the distribution) for Siberia and Alaska, while for India the 1-D reference model (SYL1) has a baseline shift so that the corresponding mean values are $\langle \delta T_{Scd-S} \rangle_{SYL1} \sim 1.7$, $\langle \delta T_{ScS-Scd} \rangle_{SYL1} \sim -1.8$ and $\langle \delta T_{ScS-S} \rangle_{SYL1} \sim -0.1$. For the purposes of our analysis, however, we choose to use the median estimates as they are more robust and tolerant to points with large departures from the bulk of the set, such as are expected in the case of misidentified phases. The median of the differential travel times for Siberia and Alaska approximately coincide with the mean estimates and are equal to zero. In the case of

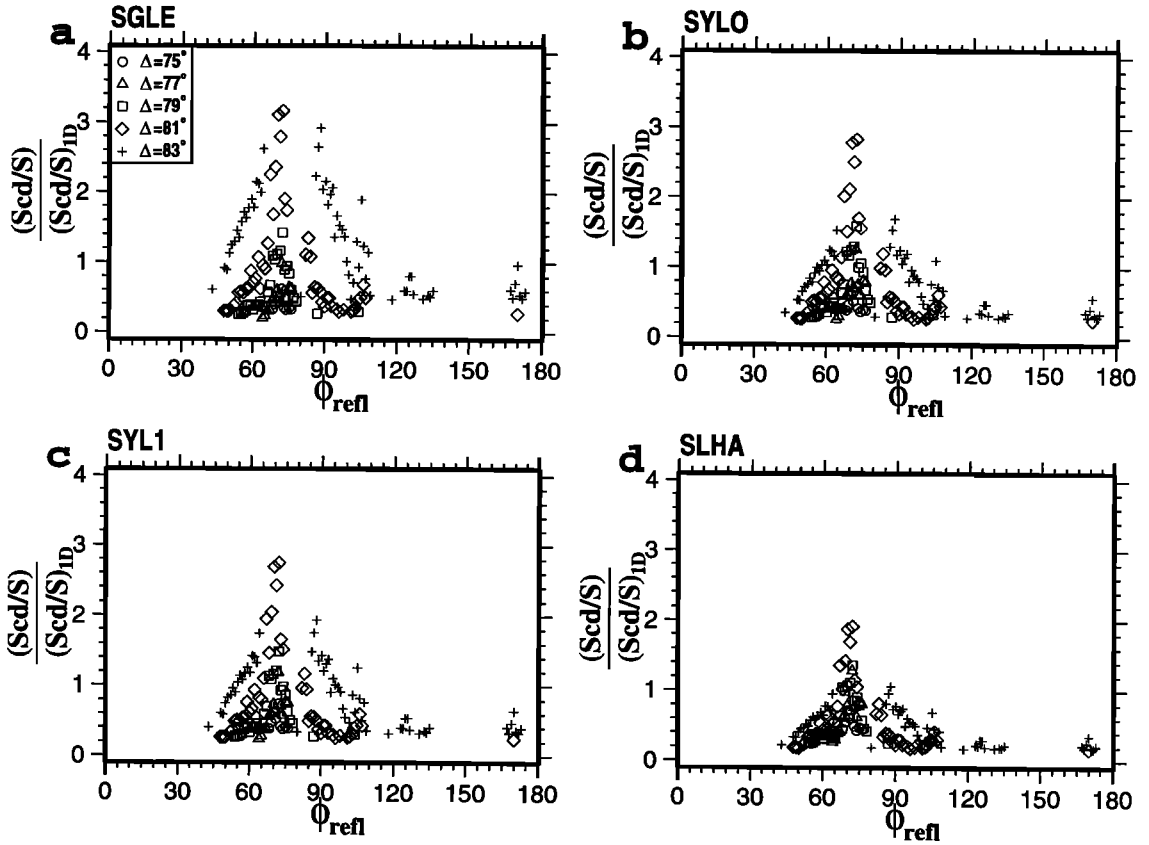

Figure 5. *Scd/S* amplitude ratios computed for the model with $\Delta\rho_{\rm ph}/\rho_0 = 0$, $\gamma_{\rm ph} = 6$ MPa K^{-1}, and $h_{\rm ph} = 150$ km. The amplitude ratios are normalized by the respective ratios (for the corresponding epicentral distances) for four different 1-D reference models: (a) SGLE, (b) SYLO, (c) SYL1, and (d) SLHA. The amplitudes are plotted as a function of the *ScS* bounce point coordinate $\phi_{\rm refl}$, with different symbols corresponding to different epicentral distances.

India the medians of the differential travel times with respect to model SYL1 are $m_e\,(\delta {\rm T}_{Scd-S})_{\rm SYL1} = 1.5$, $m_e\,(\delta {\rm T}_{ScS-Scd})_{\rm SYL1} = -1.5$, and $m_e\,(\delta {\rm T}_{ScS-S})_{\rm SYL1} = 0.3$. A study for the Central America [*Lay and Helmberger*, 1983] suggests that model SLHA has no baseline shift and that the differential travel times have zero medians.

Using these estimates, summarized in Table 2, we introduce parameter $\Delta M_1^{\rm T}$ as

$$\Delta M_1^{\rm T}({\rm model, refl D}) = \frac{1}{\sqrt{3}}\left\{\sum_{X=\{Scd-S,\,ScS-Scd,\,ScS-S\}}\left[m_e\,(\delta {\rm T}_X)_{\rm model} - m_e\,(\delta {\rm T}_X)_{\rm refl D}\right]^2\right\}^{1/2} \quad (22)$$

This parameter serves as a measure of the average shift between the median travel times from a computed model and the data (characterized by the reference 1-D model refl D). Large values of $\Delta M_1^{\rm T}$ correspond to a large shift between the median travel times for the computed model and the data for a particular region.

Similar to the approach used by *Lay et al.* [1997] for regional data, in Figure 6 we present the correlations of the differential travel times for a model with a passive phase and $\gamma_{\rm ph} = 6$ MPa K^{-1} and $h_{\rm ph} = 150$ km. Such representation of the travel times scatter is informative because it allows us to make comparisons between the travel times for a computed model and for a particular geographical region. First, the shift of the medians of the computed travel times (represented by large solid circles) from the respective medians for the data (Table 2) characterizes the baseline shift for the computed model. Second, implications can be derived from the analysis of the correlations of the individual travel times. Finally, the scatter of the travel times around the medians presents an important characteristic of the structure producing the waveforms and can be used to compare models. We characterize this scatter by the difference, $\Delta_{90\%}(\delta T_X)$, between the 95% and 5% quantiles of the distribution, which is computed by stripping 5% of the smallest and 5% of largest values in the data set and taking the range of variation in the remaining 90%. We prefer this measure of scatter to the more common variance for the same reasons as we chose medians over the means: higher robustness and tolerance to misidentified phases. We estimate the values of

Table 2. Median Values of the Seismologically Observed Differential Travel Times Distribution Around the 1-D Reference Models for the Corresponding Regions.

Geographic Region	Reference 1-D Model	$m_e\,(\delta T_{Scd-S})$, s	$m_e\,(\delta T_{ScS-Scd})$, s	$m_e\,(\delta T_{ScS-S})$, s
Northern Siberia[a]	SGLE	0	0	0
Alaska[a]	SYLO	0	0	0
India[a]	SYL1	1.5	−1.5	0.3
Central America[b]	SLHA	0	0	0

[a]Medians estimated using the data from *Lay et al.* [1997].
[b]Medians estimated using the data from *Lay and Helmberger* [1983].

$\triangle_{90\%}(\delta T_X)$ for the data in northern Siberia, Alaska, and India from the analysis presented by *Lay et al.* [1997]. The value of $\triangle_{90\%}(\delta T_{ScS-Scd})$ for the Central America region is estimated from the results of *Lay and Helmberger* [1983], and the results of *Lay* [1983] are used to derive the value of $\triangle_{90\%}(\delta T_{ScS-S})$ for that region. No analysis of *Scd-S* travel times has been performed for Central America so the value of $\triangle_{90\%}(\delta T_{Scd-S})$ for the region is chosen to keep the approximate proportions between the various travel time scatters that are observed for the other three regions.

Table 3 lists the values of $\triangle_{90\%}(\delta T_X)$ for the four geographical regions. To characterize the difference in scatter of the travel times produced by the computed structure and the data in a particular geographic region, we introduce parameter $\triangle M_2^{\mathrm{T}}$ as

$$\triangle M_2^{\mathrm{T}}(\mathrm{model},\mathrm{ref1D}) = \frac{1}{\sqrt{3}}\left\{\sum_{X=\{Scd-S,ScS-Scd,ScS-S\}}\left[\triangle_{90\%}(\delta \mathrm{T}_X)_{\mathrm{model}} - \triangle_{90\%}(\delta \mathrm{T}_X)_{\mathrm{ref1D}}\right]^2\right\}^{1/2} \quad (23)$$

Models that produce significantly smaller or larger differential travel time scatter than is observed in a given region characterized by a reference model ref1D will have larger values of $\triangle M_2^{\mathrm{T}}(\mathrm{model},\mathrm{ref1D})$ than models that produce scatter of about the same amplitude.

Using parameters $\triangle M_1^{\mathrm{A}}$, $\triangle M_1^{\mathrm{T}}$, and $\triangle M_2^{\mathrm{T}}$, we introduce a penalty function

$$p(\mathrm{model},\mathrm{ref1D}) = \frac{1}{3}\left[\widehat{\triangle M_1^{\mathrm{A}}}(\mathrm{model},\mathrm{ref1D}) + \widehat{\triangle M_1^{\mathrm{T}}}(\mathrm{model},\mathrm{ref1D}) + \widehat{\triangle M_2^{\mathrm{T}}}(\mathrm{model},\mathrm{ref1D})\right] \quad (24)$$

that characterizes the overall statistical misfit between a computed model and seismic data. It allows us to compare any two models in a class of computed models in terms of statistical proximity to the data in a given region of the world. The lower the value of $p(\mathrm{model},\mathrm{ref1D})$ for a given model, the better the fit the model provides to the seismic data observed in the region characterized by the 1-D reference model ref1D.

Parameters $\widehat{\triangle M_1^{\mathrm{A}}}$, $\widehat{\triangle M_1^{\mathrm{T}}}$, and $\widehat{\triangle M_2^{\mathrm{T}}}$ in (24) represent the normalized values of $\triangle M_1^{\mathrm{A}}$, $\triangle M_1^{\mathrm{T}}$ and $\triangle M_2^{\mathrm{T}}$, respectively. The normalization is performed for a class of computed models to ensure that parameters (21)-(23) in (24) vary in the range from 0 to 1 and thus have equal weights in the penalty function.

3.3. Comparison Results

The penalty function introduced above presents a comparison criterion, on the basis of which any two computed models can be compared in relation to the quality of fit of predicted waveforms to the regional data. In Figure 7 we plot the comparison results for the models that have been computed. As a passive phase change does not produce any dynamic effects on the flow, a single convection model can be used to study in detail the influence of parameters γ_{ph} and h_{ph} on the resulting seismic structure and the corresponding waveforms. The solid circles in Figure 7 represent models computed for $\triangle\rho_{\mathrm{ph}}/\rho_0 = 0$ (passive phase), and the open circles correspond to the few models where the high-pressure phase is 1% denser than the lower-pressure phase. The difference in the penalty functions for models with a passive phase and a denser phase is rather small for the same values of γ_{ph} and h_{ph}, which is seen clearly in Figure 7, where the adjacent solid and open circles have similar sizes. This is in agreement with our observation of the small effect of a minor (1%) density increase in the phase transition on the dynamics of the slab discussed earlier.

Variations in γ_{ph} and h_{ph}, on the other hand, lead to stronger variations in the seismic structure and the resulting waveforms. As Figure 7 suggests, a preference should be given to phase changes with a positive value of Clapeyron slope of $\sim$ 6 MPa K^{-1} and an elevation of $\sim$ 150 km above CMB under adiabatic conditions. A positive value of Clapeyron slope corresponds to exothermic phase changes, where latent heat is released when the phase change occurs. Such phase changes present a barrier to rising plumes, as when the phase change occurs in a rising plume, the latent heat is

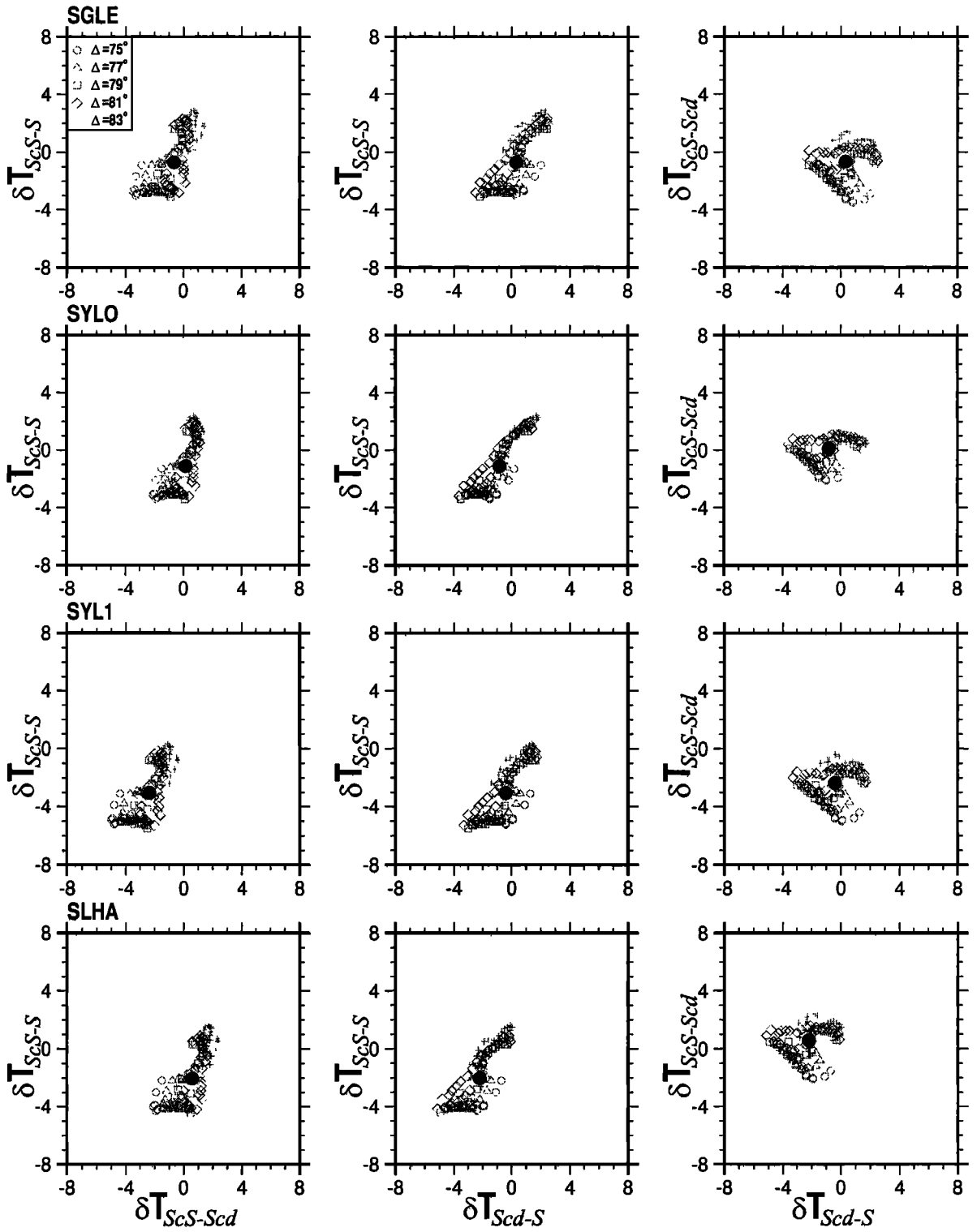

Figure 6. Correlation of differential travel times (in seconds) for a model with a passive phase and $\gamma_{ph} = 6$ MPa K^{-1} and $h_{ph} = 150$ km. The travel times were computed for five different epicentral distances (indicated by different symbols) for all the raypaths with $50° < \phi_{refl} < 90°$ and differenced with four different 1-D reference models. The large circles correspond to the median values.

Table 3. Scatter (Difference Between the 95% and 5% Quantiles) of the Differential travel times in the Different Geographical Regions

Geographic region	Reference 1-D model	$\Delta_{90\%}(\delta T_{Scd-S})$, s	$\Delta_{90\%}(\delta T_{ScS-Scd})$, s	$\Delta_{90\%}(\delta T_{ScS-S})$, s
Northern Siberia[a]	SGLE	6.5	4.5	5.5
Alaska[a]	SYLO	6.0	4.5	4.5
India[a]	SYL1	5.0	3.5	5.5
Central America	SLHA	6.5[b]	5.0[c]	6.0[d]

[a]Scatter estimated using the data from *Lay et al.* [1997].
[b]Assumed value.
[c]Estimated using the data from *Lay and Helmberger* [1983].
[d]Estimated using the data from *Lay* [1983].

consumed, which leads to the plume losing some of its buoyancy. The higher the temperature, the higher the pressure at which such a phase change occurs. Negative values of Clapeyron slope correspond to endothermic phase changes, where latent heat is consumed. Such phase changes present barriers to downwellings (slabs), and for higher temperatures the phase transition pressure is lower. The absolute value of the Clapeyron slope characterizes the variation of the depth of the discontinuity with temperature.

Our best estimate of the elevation of the phase change above the CMB (150 km) corresponds to roughly 127 GPa and 2650 K on a (P, T) diagram. Models with these characteristics provide the best fit to the structure under northern Siberia (model SGLE), closely followed by the structure under Alaska (model SYLO). The match for the structures under India and Central America is significantly worse.

3.4. Analysis of the Predicted Heterogeneity

To explore the scale lengths of the heterogeneity in our computed models, we use a method of *Lavely et al.* [1986] that was recently applied by *Lay et al.* [1997] to the data in three different regions. The idea behind the method is to approximate the spectrum of the mantle heterogeneity by a spatial autocorrelation function of the travel times residuals. This is done by computing the mean and variance of the travel time residuals between all ray paths with a given lateral separation of the *ScS* reflection points. The mean residuals and their standard deviations are plotted in Figure 8a as a function of the separation of the reflection points for a model with a passive phase and $\gamma_{\rm ph} = 6$ MPa K^{-1} and $h_{\rm ph} = 150$ km. A straightforward comparison with the analogous plots presented by *Lay et al.* [1997] for the ray paths sampling northern Siberia and Alaska is plagued by the 2-D nature of our models. Indeed, any observed low wavelength trends in the spatial correlation function cannot be expected to be reproduced by our models as a small separation between the *ScS* reflection points implies a closeness of the ray paths in 2-D geometry, while in a 3-D case the velocity structure sampled by the two paths off the vertical plane defined by the reflection points can be quite different. So, the low power in the short wavelength part of the correlation functions in Figure 8 is not surprising. Another important difference between our results for the computed models and the data analysis of *Lay et al.* [1997] is the much higher value of the standard deviation of the travel time residuals suggested by our models. However, with all the limitations of our models the analysis of the spatial correlations reveals several important trends, such as the peak at 15°-20° observed for *ScS-S*, *ScS-Scd*, and *Scd-S* residuals. This peak is relatively sharp for *ScS-S* and *Scd-S* residuals and is somewhat broader for the *ScS-Scd* residuals. Analysis of the slab structure in Figure 2a suggests that this characteristic scale of heterogeneity may reflect the folding pattern of the horizontally lying slab where the separation between adjacent folds approximately corresponds to the location of the maxima in the autocorrelation functions (Figure 8a).

Another interesting observation that can be made from Figure 8a is the relatively flat autocorrelation function for *ScS-Scd* residuals. This agrees with the results of the spatial correlation study of the travel time residuals performed by *Lay et al.* [1997] and has been interpreted as indicative of a significant heterogeneity at short scales. The relatively small amplitudes of the *ScS-Scd* autocorrelation function are in accord with the results presented in Figure 6, where the *ScS-Scd* differential travel time residuals display less scatter than the *ScS-S* and *Scd-S* residuals. This is again in good agreement with the observations [*Lay et al.*, 1997] and implies that most of the heterogeneity in the D" is concentrated just above the discontinuity or in a thin layer just below it, in a region that is sampled by both *ScS* and *Scd* ray paths.

The spatial correlation analysis also allows us to decouple the effects of the discontinuity topography variations from the volumetric heterogeneity. This can be done by repeating the correlation analysis for a model with a flat phase boundary with its elevation above the CMB equal to the average elevation of the phase boundary in the model with $\gamma_{\rm ph} = 6$ MPa K^{-1} and $h_{\rm ph} = 150$ km. The autocorrelation functions for such

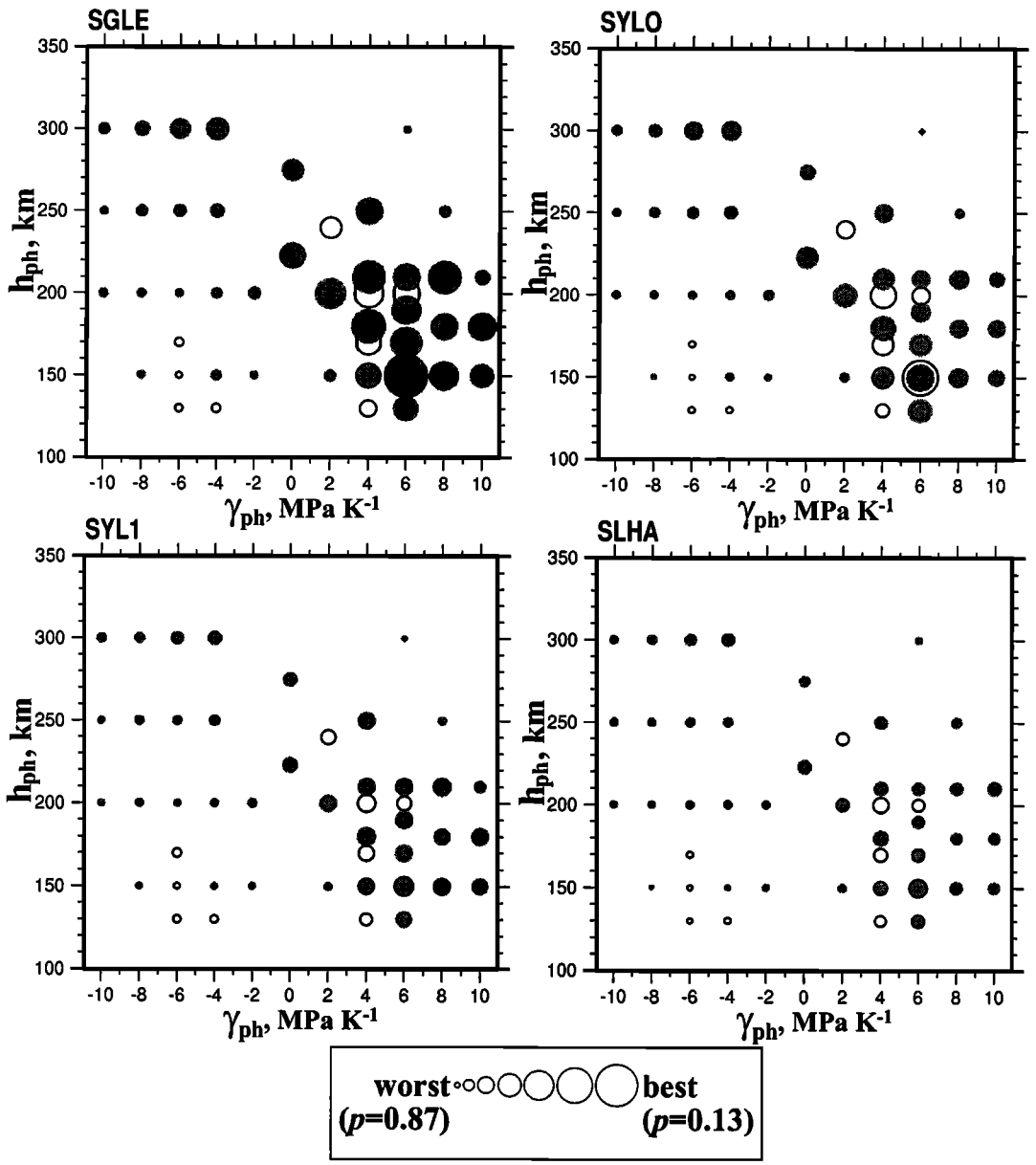

Figure 7. Comparison of computed models with different phase change characteristics. Each circle represents a model, with the size inversely proportional to the penalty function for that model and one of the four (SGLE, SYLO, SYL1 and SLHA) 1-D reference models. The larger the circle, the better the fit the model provides to the data for a given geographical region characterized by the 1-D reference model. Solid circles correspond to models with a passive phase change; open circles represent models where the high-pressure phase is 1% denser than the low-pressure phase. The value of the penalty function varies from 0.13 for the "best" model to 0.87 for the "worst" model.

a model, characterized by $\gamma_{ph} = 0$ and $h_{ph} = 223$ km, are presented in Figure 8b. Comparison of Figures 8b and Figure 8a reveals some minor differences in the *ScS-S* and *Scd-S* autocorrelations, with more pronounced changes in the trends of the *ScS-Scd* spatial correlation. This comparison suggests that the volumetric anomalies have the dominant effect on the computed *ScS-S* and *Scd-S* travel times. Even for the *ScS-Scd* autocorrelation function, the change caused by including topography variations into the seismic velocity field is within the standard error of the travel time residuals and thus cannot be considered statistically meaningful.

4. Discussion

Most purely seismological models explaining the D" triplication use a value of 2-3% for the amplitude of the shear velocity jump. On the basis of the dynamic implications for the structures at the base of the mantle, *Sidorin et al.* [1998] suggested that the triplication is

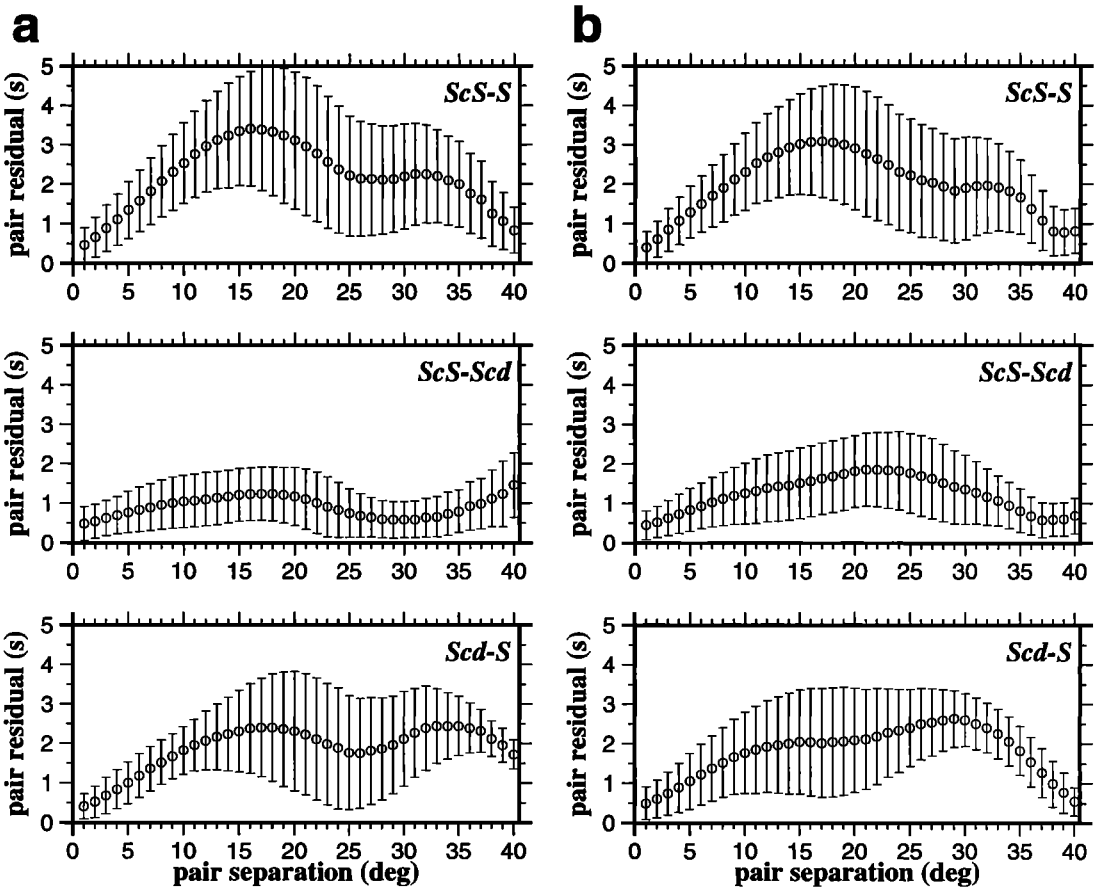

Figure 8. Spatial correlation of the differential travel time residuals for two computed models. The travel times were obtained from seven different constant offset sections corresponding to distances Δ from 75° to 83°, and residuals were computed with respect to the reference model SGLE. The circles represent the mean absolute values of residuals for all pairs of ray paths with a given separation between the *ScS* reflection points and $50° \leq \phi_{\text{refl}} \leq 90°$. The standard error is indicated by the vertical bars. (a) correlations for a model with a passive phase and $\gamma_{\text{ph}} = 6$ MPa K^{-1} and $h_{\text{ph}} = 150$ km; (b) for a model with a passive phase with a phase boundary having constant height above the CMB ($\gamma_{\text{ph}} = 0$ and $h_{\text{ph}} = 223$ km) equal to the average height of the phase boundary for the model used in Figure 8a, computed in the region $50° \leq \phi_{\text{refl}} \leq 90°$.

conditioned by both the discontinuous velocity increase and the velocity gradient just above the discontinuity and demonstrated that a model with just a 1% velocity jump overlaid by a higher than PREM gradient can explain the triplication observations under the Western Caribbean at least as well as models with a 3% discontinuity. The double structure in this class of models naturally emerges from the thermal and possibly chemical complexity of the region that gives rise to large variations in the velocity gradients and can explain the intermittent nature of the D" triplication. Although the discontinuity may be a ubiquitous feature, *Scd* arrivals of sufficient amplitude will only be observed in the regions where the discontinuity is overlaid by a significantly high velocity gradient. Such regions with high positive radial gradients of the shear velocity are expected, for example, in the areas of subduction, where the best observations of the *Scd* phase have been made.

While a phase change is a plausible mechanism for the velocity discontinuity, other possibilities exist. A simple global chemical layer at the bottom of the mantle is an unlikely candidate as a quite complex change in chemistry may be required to both dynamically stabilize the layer and make it seismically faster than the overlying mantle [*Sidorin and Gurnis,* 1998]. In addition, the geographical pattern of predicted *Scd* arrivals does not agree with the seismological observations. However, the chemical contrast caused by oceanic crust within subducted slabs may provide the required velocity jump and can be a viable alternative to the global phase change.

A phase change mechanism has previously been hypothesized as the cause of the D" discontinuity [see *Wysession et al.* 1998]. However, despite remarkable advances in the experimental mineral physics, little is known about the phase diagrams of the lower mantle

minerals. Even for the major constituents (silicate perovskite and magnesiowüstite), the questions of stability under the D" conditions remain a subject of debate. The suggestion of instability of silicates at high pressures dates back to *Birch* [1952] and was more recently supported by *Stixrude and Bukowinski* [1990] and *Meade et al.* [1995], who demonstrated that silicate perovskite dissociates into SiO_2 and (Mg,Fe)O under the conditions pertinent to the D" region. However, other studies, including theoretical calculations [*Stixrude and Cohen,* 1993] as well as experimental work [*Knittle and Jeanloz,* 1987; *Tsuchida and Yagi,* 1989; *Serghiou et al.,* 1998] argue against such a decomposition and suggest that (Mg,Fe)SiO_3-perovskite is stable under the lower mantle conditions. The existence of any phase transition under D" condition for magnesiowüstite, the other major element in the composition of the lower mantle, is also uncertain. Although FeO experiences at least one phase change in the range of pressures and temperatures corresponding to the lower mantle [*Jeanloz and Ahrens,* 1980], no evidence for a phase change has been observed for $Mg_{0.6}Fe_{0.4}O$ under shock compression up to 200 GPa [*Vassiliou and Ahrens,* 1982]. The uncertainty in the experiments conducted under simultaneous high-pressure and high-temperature conditions is such that it does not currently allow one to categorically rule out a phase transition in either silicate perovskite or magnesiowüstite under D" conditions. This is especially true because the results of this study and the study by *Sidorin et al.* [1998] suggest that a minor change in the elastic properties will suffice to explain the D" seismic triplication.

Another possible explanation for the discontinuous increase in the shear velocity atop D" is a phase transition in some of the minor constituents of the lower mantle. A consideration of the cosmic abundances suggests substantial amounts of CaO and Al_2O_3 in the lower mantle. This is probably especially true for the base of the mantle, where a higher concentration of refractory elements is expected [*Ruff and Anderson,* 1980]. Phase transitions have been discovered in both CaO and Al_2O_3 [*Jeanloz and Ahrens,* 1980; *Funamori and Jeanloz,* 1997]. The transformation of corundum (α-Al_2O_3) to the Rh_2O_3 (II) structure occurs under conditions comparable to those expected at the top of D", while the B1→B2 transition in CaO has been observed at mid mantle pressures ($\sim$ 70 GPa). However, the abundances of free CaO or Al_2O_3 at the base of the mantle are unknown. Moreover, not only is the elements partitioning between various phases under the D" conditions unknown, the relative concentrations of the elements are highly uncertain as well and depend on the model of Earth differentiation and history of mantle evolution. It seems impossible, however, to rule out a phase transformation in one of the Al- or Ca-bearing phases that would lead to a 1% increase in the shear velocity of the mineral assemblage.

A phase transition in stishovite or one of the postrutile phases of SiO_2 [*Tsuchida and Yagi,* 1989; *Dubrovinsky et al.,* 1997] is a yet another candidate for the discontinuous velocity increase atop D". It has been suggested [*Knittle and Jeanloz,* 1991; *Kellogg and King,* 1993] that the chemical reactions between the core and mantle material may increase the concentration of free silica at the base of the mantle and thus a notable phase transition in silica may, in principal, produce a sufficient increase in the shear velocity of the mineral assemblage.

Our study could not provide any constraints on the density change associated with the phase transformation that is a potential cause of the D" discontinuity. As we have demonstrated, the computed waveforms are to a large degree controlled by the slab structure, which is only slightly sensitive to the small (0-1%) density change in the phase transformation. A significantly higher density change would probably have a more important impact on the slab dynamics but is unlikely. The structure of the major lower mantle constituents (Mg, Fe perovskite, and magnesiowüstite) is already very closely packed, and any large volume change associated with further structural modifications is hardly possible. In addition, these two minerals have been a subject of a great number of high-pressure experiments, and it is unlikely that a major phase transformation with a large volume change may have been overlooked. If the phase transformation is to occur in some of the minor elements of the mineral assemblage, it may require a very large density change in order to increase the average density by much more than 1%.

The constraints provided by the seismologically observed differential travel times and their variations allowed us to estimate the Clapeyron slope (6 MPa K^{-1}) and pressure (127 GPa) of the phase change that may give rise to the D" triplication. Our dynamic models that incorporated a phase change with these parameters provided a favorable fit to the data corresponding to northern Siberia and Alaska. The poor fit to the data in Central America and India is frustrating but understandable. The D" structure under Central America is especially complex [e.g., *Kendall and Nangini,* 1996] and can hardly be characterized by a single 1-D model (SLHA). The data coverage in India is very sparse [*Lay et al.,* 1997], so that the reference model (SYL1) may also be a poor representation of the "average" structure and the actual observations.

Our study suggests that at least for a 1% velocity contrast associated with the phase transformation most of the travel time variations are due to the volumetric anomalies. The largest of these anomalies is produced by the buckling and folding of the slab lying on the core-mantle boundary. This "topography" of the thermal signature of the slab is responsible for the topography of the phase boundary, and together, they determine the variations in the differential arrival times. This explains why the variations in *ScS-Scd* residuals are relatively small: both *Scd* and *ScS* sample the same largely heterogeneous region at the top of D".

A study by *Griffiths and Turner* [1988] demonstrated that the characteristic wavelength of slab folding is primarily controlled by the rheology of the slab and the kinematics of subduction. If our interpretation of the maxima in the autocorrelation functions (Figure 8) is correct and the peak at 15°-20° indeed corresponds to the characteristic wavelength of the slab buckling, it is possible that the maxima in the autocorrelation function for the seismic data [*Lay et al.,* 1997] reflect the same physical processes. This information can then be used to constrain the rheology of the slab in the deep mantle, creating yet another loop of mutual constraints between geodynamics, mineral physics, and seismology.

5. Conclusions

Using dynamical models with a phase change near the bottom of the mantle we obtained constraints on the characteristics of the phase change (P,T conditions and Clapeyron slope) that produce seismic structures and waveforms consistent with seismological observations. We found that dynamic models that provide the best fit to the seismic observations have a Clapeyron slope of the basal phase transition of $\sim$ 6 MPa K^{-1} and an elevation of the phase boundary above the CMB of $\sim$ 150 km under adiabatic temperatures. Dynamic models indicate that a phase boundary characterized by a negative Clapeyron slope is generally smoother than a phase boundary with a positive Clapeyron slope of the same absolute value. This reduced topography of phase boundaries with a negative Clapeyron slope produces variations in seismic differential travel times that are too small and inconsistent with observations. Likewise, phase changes with a too small ($<<$ 6 MPa K^{-1}) or too large ($>>$ 6 MPa K^{-1}) positive Clapeyron slope lead to too small or excessively large variations of differential travel times.

We found that the D" discontinuity modeled by the phase change in our computations produces the strongest triplication in the area of subduction and weak or absent *Scd* arrivals away from the slab. This pattern is consistent with the general geographical pattern of the D" triplication observations, where the strongest *Scd* arrivals have been reported in subduction areas. The dynamics of the slab appears to be important in giving rise to the triplication, as the thermal structure of the slab produces volumetric seismic velocity anomalies and modifies the topography of the discontinuity. These anomalies and the phase boundary topography explain most of the variations in the differential travel times. The patterns in these variations, such as relatively small amplitude of *ScS-Scd* variations, are consistent with the results obtained by *Lay et al.* [1997] for the data in various regions and indicate that the largest heterogeneity is located at the very top of the D" layer or just above it. The characteristic peaks in the spatial autocorrelation functions of seismic differential travel time residuals may be representative of the characteristic wavelengths of folding of subducted slabs. If so, the analysis of spatial correlations of the seismic travel time anomalies may provide important constraints on the rheology of the slab at the base of the mantle.

Our analysis failed to provide any constraints on the density change associated with the phase transition that may be responsible for the D" discontinuity. Although the density change, together with Clapeyron slope, has a significant influence on the dynamics of plumes emerging from the CMB, its impact on the dynamics of subducting slabs is minor, which can be partly due to slab kinematics enforced in our models. Fully dynamic models of subduction with a more realistic rheology would be required to investigate further the general influence of this parameter. Plate kinematics, effects of internal heating, rheology, and other factors to some extent control the dynamics of the system and thus the seismic velocity field at any point in its evolution. However, the analysis of these parameters is out of the scope of this study and is left for future investigation. Although a phase change appears to be a viable mechanism for the D" seismic discontinuity, other possibilities, such as the chemical contrast associated with the subducted oceanic crust in slabs, cannot be ruled out and deserve further study.

Acknowledgments. This study was supported by NSF grants EAR9629279 and EAR9809771. This represents contribution 8550 of the Division of Geological and Planetary Sciences, California Institute of Technology.

References

Birch, F., Elasticity and constitution of the Earth's interior, *J. Geophys. Res., 57,* 227–286, 1952.

Breuer, D., D. A. Yuen, T. Spohn, and S. Zhang, Three-dimensional models of Martian mantle convection with phase transitions, *Geophys. Res. Lett., 25,* 229–232, 1998.

Bunge, H. P., M. A. Richards, C. Lithgow-Bertelloni, J. R. Baumgardner, S. P. Grand, and B. A. Romanowicz, Time scales and heterogeneous structure in geodynamic Earth models, *Science, 280,* 91–95, 1998.

Christensen, U., Convection with pressure- and temperature-dependent non-Newtonian rheology, *Geophys. J. R. Astron. Soc., 77,* 343–384, 1984.

Christensen, U. R., The influence of trench migration on slab penetration into the lower mantle, *Earth Planet. Sci. Lett., 140,* 27–39, 1996.

Christensen, U. R., and D. A. Yuen, The interaction of a subducting lithospheric slab with a chemical or phase boundary, *J. Geophys. Res., 89,* 4389–4402, 1984.

Davies, G. F., Incorporating plate into mantle convection models (abstract), Chapman Conference on the History and Dynamics of Global Plate Motions, p. 42, AGU, Washington, D.C., 1997.

Ding, X., and D. V. Helmberger, Modeling D" structure beneath Central America with broadband seismic data, *Phys. Earth Planet. Inter., 101,* 245–270, 1997.

Dubrovinsky, L. S., S. K. Saxena, P. Lazor, R. Ahuja, O. Eriksson, J. M. Wills, and B. Johansson, Experimental and theoretical identification of a new high-pressure phase of silica, *Nature, 388,* 362–365, 1997.

Dziewonski, A. M., and D. L. Anderson, Preliminary reference Earth model, *Phys. Earth Planet. Inter., 25,* 297–356, 1981.

Dziewonski, A. M., and J. H. Woodhouse, Global images of the Earth's interior, *Science, 236,* 37–48, 1987.

Funamori, N., and R. Jeanloz, High-pressure transformation of Al_2O_3, *Science, 278,* 1109–1111, 1997.

Gaherty, J. B., and T. Lay, Investigation of laterally heterogeneous shear velocity structure in D" beneath Eurasia, *J. Geophys. Res., 97,* 417–435, 1992.

Garnero, E. J., and D. V. Helmberger, A very slow basal layer underlying large-scale low-velocity anomalies in the lower mantle beneath the Pacific: Evidence from core phases, *Phys. Earth Planet. Inter., 91,* 161–176, 1995.

Grand, S. P., Mantle shear structure beneath the Americas and surrounding oceans, *J. Geophys. Res., 99,* 11,591-11,622, 1994.

Grand, S. P., R. D. van der Hilst, and S. Widiyantoro, Global seismic tomography: A snapshot of convection in the Earth, *GSA Today, 7,* 1–7, 1997.

Griffiths, R. W., and J. S Turner, Folding of viscous plumes impinging on a density or viscosity interface, *Geophys. J., 95,* 397–419, 1988.

Gurnis, M. and G. F. Davies, Mixing in numerical models of mantle convection incorporating plate kinematics, *J. Geophys. Res., 91,* 6375–6395, 1986.

Han, L., and M. Gurnis, How valid are dynamic models of subduction and convection when plate motions are prescribed?, *Phys. Earth Planet. Inter., 110,* 235–246, 1999.

Jeanloz, R., and T. J. Ahrens, Equations of state of FeO and CaO, *Geophys. J. R. Astron. Soc., 62,* 505–528, 1980.

Kellogg, L. H., and S. D. King, Effect of mantle plumes on the growth of D" by reaction between the core and mantle, *Geophys. Res. Lett., 20,* 379–382, 1993.

Kendall, J.-M., and C. Nangini, Lateral variations in D" below the Caribbean, *Geophys. Res. Lett., 23,* 399–402, 1996.

King, S. D., A. Raefsky, and B. H. Hager, ConMan: Vectorizing a finite element code for incompressible two-dimensional convection in the Earth's mantle, *Phys. Earth Planet. Inter., 59,* 195–207, 1990.

Knittle, E., and R. Jeanloz, Synthesis and equation of state of $(Mg,Fe)SiO_3$ perovskite to over 100 gigapascals, *Science, 235,* 668–670, 1987.

Knittle, E., and R. Jeanloz, Earth's core-mantle boundary: Results of experiments at high pressures and temperatures, *Science, 251,* 1438–1443, 1991.

Lavely, E. M., D. W. Forsyth, and P. Friedemann, Scales of heterogeneity near the core-mantle boundary, *Geophys. Res. Lett., 13,* 1505–1508, 1986.

Lay, T., Localized velocity anomalies in the lower mantle, *Geophys. J. R. Astron. Soc., 72,* 483–516, 1983.

Lay, T., and D. V. Helmberger, A lower mantle S-wave triplication and the shear velocity structure of D", *Geophys. J. R. Astron. Soc., 75,* 799–838, 1983.

Lay, T., E. J. Garnero, C. J. Young, and J. B. Gaherty, Scale lengths of shear velocity heterogeneity at the base of the mantle from *S* wave differential travel times, *J. Geophys. Res., 102,* 9887–9909, 1997.

Lay, T., Q. Williams, and E. J. Garnero, The core-mantle boundary layer and deep Earth dynamics, *Nature, 392,* 461–468, 1998.

Li, X. D., and B. Romanowicz, Global mantle shear velocity model developed using nonlinear asymptotic coupling theory, *J. Geophys. Res., 101,* 22,245–22,272, 1996.

Masters, G., S. Johnson, G. Laske, and H. Bolton, A shear-velocity model of the mantle, *Philos. Trans. R. Soc. London A, 354,* 1385–1411, 1996.

Meade, C., H. K. Mao, and J. Hu, High temperature phase transition and dissociation of $(Mg,Fe)SiO_3$ perovskite at lower mantle pressures, *Science, 268,* 1743–1745, 1995.

Ni, S., X. Ding, and D. V. Helmberger, Constructing synthetics for deep Earth tomographic models, *Geophys. J. Int.,* in press, 1999.

Ruff, L., and D. L. Anderson, Core formation, evolution, and convection: A geophysical model, *Phys. Earth Planet. Inter., 21,* 181–201, 1980.

Serghiou, G., A. Zerr, and R. Boehler, $(Mg,Fe)SiO_3$-perovskite stability under lower mantle conditions, *Science, 280,* 2093–2095, 1998.

Sidorin, I., and M. Gurnis, Geodynamically consistent seismic velocity predictions at the base of the mantle, *The Core-Mantle Boundary Region, Geodyn. Ser.,* vol. 28, edited by Gurnis et al., pp. 209–230, AGU, Washington, D.C., 1998.

Sidorin, I., M. Gurnis, D. Helmberger, and X. Ding, Interpreting D" seismic structure using synthetic waveforms computed from dynamic models, *Earth Planet. Sci. Lett., 163,* 31–41, 1998.

Stixrude, L., and M. S. T. Bukowinski, Fundamental thermodynamic relations and silicate melting with implications for the constitution of D", *J. Geophys. Res., 95,* 19,311–19,325, 1990.

Stixrude, L., and R. E. Cohen, Stability of orthorhombic $MgSiO_3$ perovskite in the Earth's lower mantle, *Nature, 364,* 613–615, 1993.

Su, W., R. L. Woodward, and A. M. Dziewonski, Degree 12 model of shear velocity heterogeneity in the mantle, *J. Geophys. Res., 99,* 6945–6980, 1994.

Tsuchida, Y., and T. Yagi, A new, post-stishovite high-pressure polymorph of silica, *Nature, 340,* 217–220, 1989.

van der Hilst, R. D., S. Widiyantoro, and E. R. Engdahl, Evidence for deep mantle circulation from global tomography, *Nature, 386,* 578–584, 1997.

van Heijst, H. R., and J. Woodhouse, Global high resolution overtone and fundamental mode surface wave phase velocity distributions determined using mode branch stripping, *Geophys. J. Int.,* in press, 1999.

Vassiliou, M. S., and T. J. Ahrens, The equation of state of $Mg_{0.6}Fe_{0.4}O$ to 200 GPa, *Geophys. Res. Lett., 9,* 127–130, 1982.

Wysession, M. E., T. Lay, J. Revenaugh, Q. Williams, E. Garnero, R. Jeanloz, and L. H. Kellogg, The D" discontinuity and its implications, *The Core-Mantle Boundary Region, Geodyn. Ser.,* vol. 28, edited by Gurnis et al., pp. 273–297, AGU, Washington, D.C., 1998.

Young, C. J., and T. Lay, Evidence for a shear velocity discontinuity in the lowermost mantle beneath India and the Indian Ocean, *Phys. Earth Planet. Inter., 49,* 37–53, 1987.

Young, C. J., and T. Lay, Multiple phase analysis of the shear velocity structure in the region beneath Alaska, *J. Geophys. Res., 95,* 17,385–17,402, 1990.

Zhong, S., and M. Gurnis, Dynamic feedback between a continentlike raft and thermal convection, *J. Geophys. Res.,* 98, 12,219–12,232, 1993.

M. Gurnis, D. V. Helmberger, and I. Sidorin, Seismological Laboratory 252-21, California Institute of Technology, Pasadena, CA 91125 (gurnis@caltech.edu; helm@gps.caltech.edu; igor@gps.caltech.edu)

(Received August 24, 1998; revised February 2, 1999; accepted February 11, 1999.)